Journal of the Mechanics and Physics of Solids 59 (2011) 89–102

Contents lists available at ScienceDirect

Journal of the Mechanics and Physics of Solids

journal homepage: www.elsevier.com/locate/jmps

Multiscale mass-spring models of carbon nanotube foams

F. Fraternali [a,b,*], T. Blesgen [c], A. Amendola [a], C. Daraio [d]

[a] Department of Civil Engineering, University of Salerno, 84084 Fisciano(SA), Italy
[b] Division of Engineering, King's College London, Strand, London WC2R 2LS, UK
[c] Max-Planck-Institute for Mathematics in the Sciences, Inselstraße 22-26, D-04103 Leipzig, Germany
[d] Graduate Aerospace Laboratories (GALCIT) and Applied Physics, Engineering and Applied Sciences, California Institute of Technology, Pasadena, CA 91125, USA

ARTICLE INFO

Article history:
Received 20 April 2010
Received in revised form
9 September 2010
Accepted 11 September 2010

Keywords:
Carbon nanotube foams
Bi-stable springs
Multiscale behavior
Strain localization
Hysteresis

ABSTRACT

This article is concerned with the mechanical properties of dense, vertically aligned CNT foams subject to one-dimensional compressive loading. We develop a discrete model directly inspired by the micromechanical response reported experimentally for CNT foams, where infinitesimal portions of the tubes are represented by collections of uniform bi-stable springs. Under cyclic loading, the given model predicts an initial elastic deformation, a non-homogeneous buckling regime, and a densification response, accompanied by a hysteretic unloading path. We compute the dynamic dissipation of such a model through an analytic approach. The continuum limit of the microscopic spring chain defines a mesoscopic dissipative element (micro–meso transition) which represents a finite portion of the foam thickness. An upper-scale model formed by a chain of non-uniform mesoscopic springs is employed to describe the entire CNT foam. A numerical approximation illustrates the main features of the proposed multiscale approach. Available experimental results on the compressive response of CNT foams are fitted with excellent agreement.

1. Introduction

Since their discovery (Radushkevich and Lukyanovich, 1952; Oberlin et al., 1976; Iijima et al., 1995), carbon nanotubes (CNTs) have been widely studied to understand their chemical, electrical and mechanical responses. Because of their unique properties and their multiscale nature, forests of vertically aligned carpets of CNTs have been proposed for a variety of applications ranging from protective packaging systems to new tactile sensors (Iijima, 1991; Veedu et al., 2006; Daraio et al., 2004b; Majumder et al., 2005; Maheshwari and Saraf, 2008). The mechanical response of individual nanotubes under axial and radial deformation and their bending/buckling modes, have been studied extensively using experimental, theoretical and molecular-dynamics analysis (Iijima et al., 1995; Yakobson and Brabec, 1996; Falvo et al., 1997; Belytschko et al., 2002; Arroyo and Belytschko, 2003; Pantano et al., 2004; Cao and Chen, 2006). The elastic modulus E of individual carbon nanotubes has been reported to be very high: ~ 1 TPa (Pantano et al., 2004). However, in experiments this value can vary widely, depending on the number of defects, the CNT microstructure and the synthesis method followed.

The study of the mechanical properties of CNTs was later extended to bundles of nanotubes under pressure (Chesnokov et al., 1999; Peters et al., 2000; Chan et al., 2003; Liu et al., 2005; Qi et al., 2003) and to CNT forests under nanoindentation

* Corresponding author at: Department of Civil Engineering, University of Salerno, 84084 Fisciano(SA), Italy.
E-mail addresses: f.fraternali@unisa.it (F. Fraternali), blesgen@mis.mpg.de (T. Blesgen), adamendola@gmail.com (A. Amendola), daraio@caltech.edu (C. Daraio).

0022-5096/$ - see front matter © 2010 Elsevier Ltd. All rights reserved.
doi:10.1016/j.jmps.2010.09.004

(Mesarovic et al., 2007). The study of thin structural foams (Gibson and Ashby, 1998) for cushioning (Zhang et al., 2009), energy dissipation (Teo et al., 2007) and protection (Liu et al., 2008) has received increasing attention for several practical applications, including mitigation of explosive loading (Nesterenko, 2001). Nanotube-based films have been reported as an excellent alternative to regular foams, exhibiting a super-compressible foam-like behavior under compressive cycling loads (Suhr et al., 2007; Teo et al., 2007; Tong et al., 2008; Deck et al., 2007; Cao et al., 2005). Investigations on the dynamic response of foam-like forests of CNTs under dynamic ball impacts have also been performed (Daraio et al., 2004a,b, 2006; Misra et al., 2009). Available results show a strongly nonlinear response that appears to be very suitable for energy-absorbing layered materials in noise and shock wave mitigation and as nonlinear springs for assembling nonlinear acoustic crystals. The response of the CNT forests was also found to be strongly dependent on the forests' microstructure (height, density, alignment, etc.) and growth method. In certain cases the possible presence of plastic deformation and fracturing of the tubes was reported (Daraio et al., 2004b).

Mechanical models consisting of chains of identical bi-stable springs have been extensively studied by several authors, since they can describe a series of relevant nonlinear material behaviors (e.g., phase transformations, reversible pseudo-plasticity, hysteresis, fracture), through the interplay between macroscopic and microscopic length scales (e.g. Ortiz, 1999; Puglisi and Truskinovsky, 2000, 2002, 2005). It is well-known that such systems exhibit a 'bumpy' multi-well energy landscape, allowing for multiple metastable equilibria (cf., e.g., Blesgen, 2007; Braides and Cicalese, 2007; Charlotte and Truskinovsky, 2002, 2008; Ortiz, 1999; Puglisi and Truskinovsky, 2000, 2002). In particular, Pampolini and Del Piero (2008) have recently found that they well-describe the hysteretic response of open-cell polyurethane foams under confined compression tests.

In this article, we present a phenomenological model of the mechanical response of carbon nanotube foams under compressive loading, which is inspired by some distinctive features of the micromechanical response reported earlier (cf., e.g., Cao et al., 2005; Zbib et al., 2008; Misra et al., 2009; Hutchens et al., 2010). The given model makes use of multiscale chains of lumped masses connected by nonlinear springs. It captures the 'three-phase' compressive deformation response of CNT forests shown by a number of experimental studies. The compressive deformation response is characterized by an initial elastic deformation, a non-homogeneous buckling (or plateau) regime, often featuring a sawtooth-like profile, and a densification phase. This three-phase response, which is common for cellular materials (Gibson and Ashby, 1998), is usually accompanied by marked hysteresis and strain localization in CNT structures. We show in Section 3 that a series of bi-stable elastic springs (Fig. 1) described by the potential in Eq. (1) exhibits a similar stress–strain response (Fig. 6), and through-the-thickness localization of the axial deformation (Fig. 7). The latter effect mimics the snap-buckling events observed through Scanning Electron Microscope (SEM) in real CNT arrays (cf. Fig. 2 of Cao et al., 2005; Fig. 3 of Hutchens et al., 2010). Such a model therefore appears to be effective in describing the microstructure rearrangements taking place in compressed CNT foams, within a simple 1D framework.

We focus on the time-independent component of the hysteresis associated with the compressive loading/unloading of CNT foams, which is essentially due to effects such as friction, entanglement and electrostatic interaction between individual and bundles of carbon nanotubes (Suhr et al., 2007; Teo et al., 2007; Tong et al., 2008; Deck et al., 2007; Misra et al., 2009; Cao et al., 2005). The macroscopic hysteresis is described as a rate-independent phenomenon induced by the succession of infinitesimal viscous events at the microscopic scale (Puglisi and Truskinovsky, 2005). As a result, the mechanical model presented in this work does not account for viscosity or other rate-dependent effects at the macroscopic scale, which we address to future work.

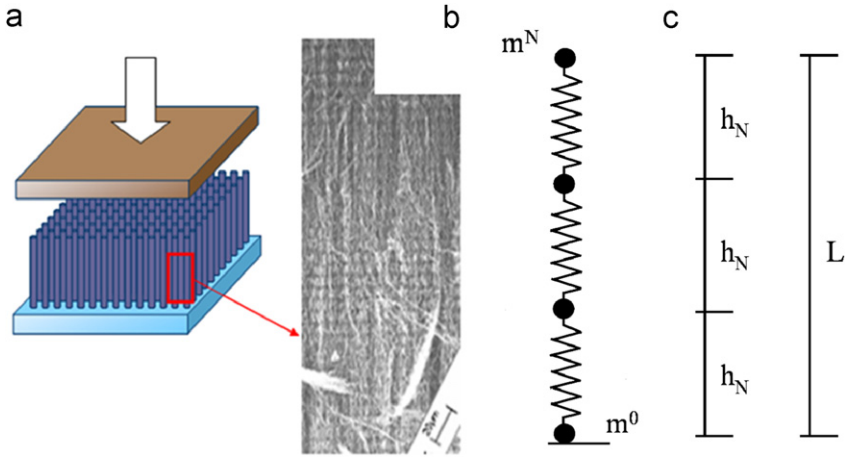

Fig. 1. (a) Schematic diagram of a vertically aligned CNT foam, uniformly loaded in compression. (b) SEM of the as-grown carbon nanotube film showing the alignment and the microstructural layering due to the growth process (Deck and Vecchio, 2005). (c) Modeling of a portion of a CNT foam as a collection of microscopic mass-spring elements.

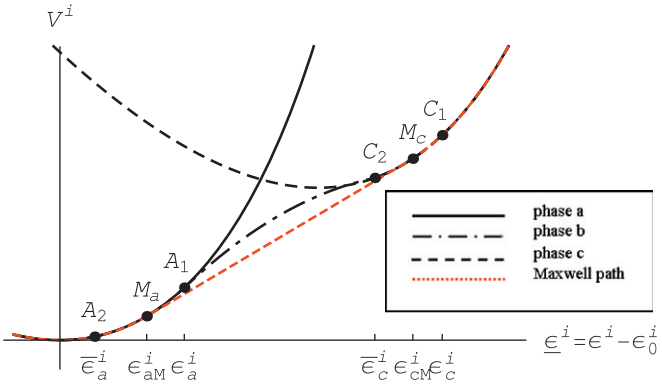

Fig. 2. Mechanical energy V^i of the generic microscopic (bi-stable) spring.

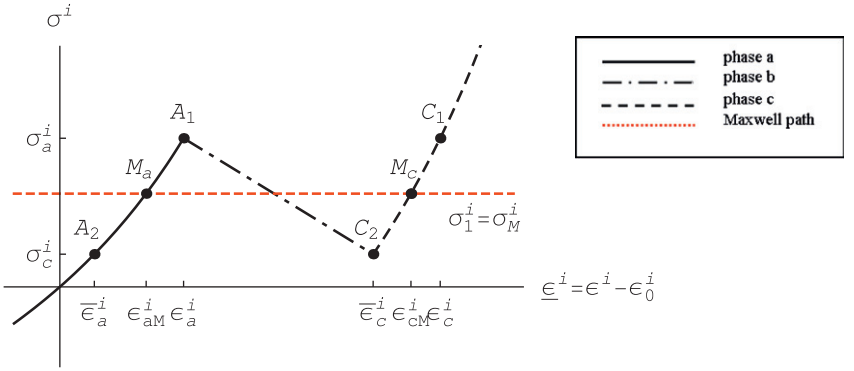

Fig. 3. Stress σ^i versus strain ε^i relationship in the generic microscopic spring.

Most of the available studies on bi-stable spring chains consider only two spatial-temporal micro–macro scales. The formulation adopted in the present study introduces instead three different time-space scales: a 'microscopic' scale (of the order of nanometers), associated with the individual bi-stable springs and an infinitesimal portion of the total foam thickness L_{tot}; a 'mesoscopic scale' (of the order of micrometers), corresponding to the limit of an infinite series of microscopic springs and representing a finite portion of L_{tot}; and a 'macroscopic' scale (of the order of millimeters), describing the entire foam. We start with the derivation of a discrete 1D model at the microscopic level, showing $N+1$ particles having nearest neighbors connected by N uniform nonlinear springs. The discrete spring potentials are chosen to allow the study of softening and strain localization of the tubes. This is discussed in Section 2. Here, we build on the concept of bi-stable springs discussed by Puglisi and Truskinovsky (2000, 2002, 2005). In Section 3 we determine analytically the continuum limit $N\to\infty$ of the microscopic spring chain, by particularizing to the present case the analysis presented in Puglisi and Truskinovsky (2005). Such a limit defines a mesoscopic dissipative element. In Section 4 we then formulate an upper scale model of the entire CNT foam through an information-passing approach by superimposing a finite number of mesoscopic dissipative springs with different mechanical properties. We account in this way for inhomogeneities induced by the CNT growth process, which several authors think to be a leading cause of the discrete folding/buckling events described above (Cao et al., 2005; Hutchens et al., 2010). The introduction of non-uniform mechanical properties allows us to enrich the formulation given in Puglisi and Truskinovsky (2000, 2002, 2005), Pampolini and Del Piero (2008) for bi-stable spring chains, modeling macroscopic hardening, instead of a perfectly 'plastic' response. Hardening-type post-buckling regimes are commonly observed in compression tests on CNT foams (Cao et al., 2005; Misra et al., 2009). We present in Section 5 a numerical micro–meso convergence study, and the fitting of mesoscopic model parameters to different available experimental data on compressed CNT foams. We demonstrate that the proposed model and its numerical implementation are capable of reproducing the physical behavior of real CNT foams with excellent agreement. We end the article with a critical evaluation and discussion of the results and an outlook.

2. The mechanical model at the microscopic scale

We model a small-scale portion of a CNT array as a collection of $N+1$ lumped masses $m^0,\ldots,m^N$ piled up one over the other (with $N>2$). In this configuration, m^0 is clamped at the bottom of the pile at the position $x^0=0$, whereas m^N is on top

at position $x^N = L > 0$, referring to the unstressed reference configuration (Fig. 1c). The nearest neighboring mass points are connected by N nonlinear microscopic springs. We assume that the reference configuration displays equal distances $h_N := L/N$ between the masses, and denote the axial displacement of the mass m^i (positive upward) by u_N^i (with u_N^0=0, see Fig. 1c). We set $u_N := \{u_N^0, \ldots, u_N^N\}$.

For the mechanical energy V^i of the microscopic spring placed between nearest neighbors m^{i-1} and m^i, we assume the three-branch expression defined by

$$V^i(\underline{\varepsilon}^i) = \begin{cases} V_a^i(\underline{\varepsilon}^i) = -k_0^i[\underline{\varepsilon}^i + \ln(1-\underline{\varepsilon}^i)], & \underline{\varepsilon}^i < \varepsilon_a^i, \\ V_b^i(\underline{\varepsilon}^i) = c_1 + \sigma_a^i \underline{\varepsilon}^i + \frac{1}{2}k_b^i(\underline{\varepsilon}^i - \varepsilon_a^i)^2, & \varepsilon_a^i \le \underline{\varepsilon}^i \le \overline{\varepsilon}_c^i, \\ V_c^i(\underline{\varepsilon}^i) = c_2 - k_c^i[\underline{\varepsilon}^i - \varepsilon_*^i + \ln(1-(\underline{\varepsilon}^i - \varepsilon_*^i))], & \overline{\varepsilon}_c^i < \underline{\varepsilon}^i, \end{cases} \tag{1}$$

with $\underline{\varepsilon}^i = \varepsilon^i - \varepsilon_0^i$, where

$$\varepsilon^i = \varepsilon^i(u_N) = \frac{u_N^{i-1} - u_N^i}{h_N} \tag{2}$$

is the strain measure associated with such a spring (positive in compression). In (1), the quantity $\varepsilon_0^i \ge 0$ determines the value of ε^i corresponding to the first minimum of V^i ('equilibrium' or 'initial' strain); $k_0^i > 0$, $k_b^i < 0$, $k_c^i > 0$, $\varepsilon_a^i > 0$ and $\varepsilon_c^i \ge \varepsilon_a^i$ are constitutive parameters (five independent parameters); the constants $c_1 < 0$ and $c_2 > 0$ are such that $V_a^i(\varepsilon_a^i) = V_b^i(\varepsilon_a^i)$, $V_b^i(\overline{\varepsilon}_c^i) = V_c^i(\overline{\varepsilon}_c^i)$; and it results

$$\varepsilon_*^i = \varepsilon_c^i - \frac{\sigma_a^i}{k_c^i + \sigma_a^i}, \tag{3}$$

$$\overline{\varepsilon}_c^i = \frac{\varepsilon_c^i(k_c^i + \sigma_a^i)}{k_c^i + \sigma_c^i} + \frac{(\sigma_c^i - \sigma_a^i)(k_c^i + \varepsilon_c^i k_c^i + \varepsilon_c^i \sigma_a^i)}{(k_c^i + \sigma_a^i)(k_c^i + \sigma_c^i)}, \tag{4}$$

with

$$\sigma_a^i = k_0^i \frac{\varepsilon_a^i}{1-\varepsilon_a^i}, \ \sigma_c^i = \sigma_a^i + k_b^i(\overline{\varepsilon}_c^i - \varepsilon_a^i). \tag{5}$$

The relationship

$$\sigma^i(\underline{\varepsilon}^i) = V^{i\prime} = \begin{cases} k_0^i \frac{\underline{\varepsilon}^i}{1-\underline{\varepsilon}^i}, & \underline{\varepsilon}^i < \varepsilon_a^i, \\ \sigma_a^i + k_b^i(\underline{\varepsilon}^i - \varepsilon_a^i), & \varepsilon_a^i \le \underline{\varepsilon}^i \le \overline{\varepsilon}_c^i, \\ \frac{k_c^i(\underline{\varepsilon}^i - \varepsilon_*^i)}{1-(\underline{\varepsilon}^i - \varepsilon_*^i)}, & \overline{\varepsilon}_c^i < \underline{\varepsilon}^i \end{cases} \tag{6}$$

defines the stress σ^i acting in the spring connecting m^{i-1} with m^i.

We deduce from (1) that V^i owes the two-well profile shown in Fig. 2. Accordingly, the stress–strain relationship (6) is described by the non-monotone profile depicted in Fig. 3. It is worth noting that the mechanical response of the generic microscopic spring encompasses two stable phases, for $\underline{\varepsilon}^i < \varepsilon_a^i$ (phase a) and $\underline{\varepsilon}^i > \overline{\varepsilon}_c^i$ (phase c), respectively; and an intermediate unstable phase b for $\varepsilon_a^i \ge \underline{\varepsilon}^i \ge \overline{\varepsilon}_c^i$ (spinodal regime). For future use, we set

$$\Delta\sigma^i := \sigma_c^i - \sigma_a^i, \quad \overline{\varepsilon}_a^i := \frac{\varepsilon_a^i \sigma_c^i}{\sigma_a^i + \varepsilon_a^i \Delta\sigma^i}, \tag{7}$$

and let σ_M^i denote the slope of the linear branch of the convex hull of V_i (Maxwell stress, see Fig. 3). We also convene to denoting the value of $\underline{\varepsilon}^i$ where $\sigma^i = \sigma_M^i$ in phase a by $\varepsilon_{a_M}^i$, and the value of $\underline{\varepsilon}^i$ such that $\sigma^i = \sigma_M^i$ in phase c by $\varepsilon_{c_M}^i$. With reference to the generic spring, Eq. $(6)_1$ highlights that k_0^i represents the elastic stiffness at zero stress in phase a ($\underline{\varepsilon}^i = 0$). On the other hand, Eq. $(6)_2$ points out that k_b^i represents the (constant) stiffness in the spinodal phase b, while Eq. $(6)_3$ reveals that k_c^i represents the stiffness at zero stress in phase c ($\underline{\varepsilon}^i = \varepsilon_*^i$). By symmetric we name the case with k_c^i=k_0^i and by 'asymmetric' the one with $k_c^i \ne k_0^i$. The meaning of the other quantities appearing in Eqs. (1)–(7) is illustrated in Figs. 2 and 3.

3. Dynamic relaxation and hysteresis at the mesoscale

There are two fundamental characteristics reported experimentally in the bulk compressive response of dense vertically aligned CNTs forests: (i) a good recovery of deformation even at large compressive strains after a sufficiently large recovery time (Cao et al., 2005; Misra et al., 2009); and (ii) a strong hysteresis, observed in particular in as-grown foams, attributed to several potential effects, including friction, entanglement and electrostatic interaction between individual and bundles of carbon nanotubes (Suhr et al., 2007; Teo et al., 2007; Tong et al., 2008; Deck et al., 2007; Misra et al., 2009; Cao et al., 2005). In the present section we will analyze such a dissipative behavior by studying a dynamic switching process at the

microscopic scale between the phases (a) and (c) described in Figs. 2 and 3. This is in line with the ideas in Puglisi and Truskinovsky (2002, 2005). Following Puglisi and Truskinovsky (2005), we name a response of the material *plastic*, if the strain ε^i of a single spring exceeds $\varepsilon_0^i+\varepsilon_a^i$. For a chain of N springs, this can be characterized by the occurrence of loading and unloading stress plateaux. However, we notice that our analysis excludes accumulation of permanent deformation, therefore the end point of one hysteresis cycle coincides with the start point of the next cycle. In this sense, the present hysteresis model is time-independent. We will show in Section 5.2 that it is nevertheless capable of capturing a previously accumulated permanent deformation (*mechanical preconditioning*), through suitable definition of the initial strains ε_0^i.

Within the current section, we rescale for simplicity L to unity, and assume that V^i is independent of the spatial position. Accordingly, we drop the superscript i in front of the spring properties. This because we refer the following analysis to a finite portion of the CNT foam, regarding such a mesoscopic element as the limit for $N\to\infty$ of a series of N identical microscopic springs. Furthermore, we restrict our attention to the case with $k_c=k_0$ ('symmetric' model), and $\varepsilon_0=0$. For the present analysis we require a certain smallness condition on ε_a and $\overline{\varepsilon}_c$ relating to strong pinning that disappears in the limit $N\to\infty$, see Puglisi and Truskinovsky (2002).

We define the mechanical energy of the foam as

$$E_N(u_N)=\frac{1}{N}\sum_{i=1}^{N}V(\varepsilon^i(u_N)), \tag{8}$$

with the effective potential

$$V(\varepsilon)=\begin{cases}-k_0[\varepsilon+\ln(1-\varepsilon)] & \text{if } \varepsilon<\varepsilon_a,\\ c_1+\sigma_a\varepsilon+\dfrac{k_b}{2}(\varepsilon-\varepsilon_a)^2 & \text{if } \varepsilon_a\le\varepsilon\le\overline{\varepsilon}_c,\\ c_2-k_0[\varepsilon-\varepsilon_*+\ln(1-\varepsilon+\varepsilon_*)] & \text{if } \overline{\varepsilon}_c<\varepsilon.\end{cases}$$

Let σ be the given total stress, coinciding at equilibrium with the stress in each individual spring ($\sigma=\sigma^1=\cdots=\sigma^N$). The total average strain is simply

$$\varepsilon(u_N):=\frac{1}{N}\sum_{i=1}^{N}\varepsilon^i(u_N).$$

We model plasticity by the gradient flow equations (Puglisi and Truskinovsky, 2005)

$$v\dot{\varepsilon}^i(u_N)=-\frac{\partial\Phi_N}{\partial\varepsilon^i}(\varepsilon^1(u_N),\ldots,\varepsilon^N(u_N)), \tag{9}$$

with the total energy

$$\Phi_N(\varepsilon^1,\ldots,\varepsilon^N):=\frac{1}{N}\sum_{i=1}^{N}[V(\varepsilon^i)-\sigma\varepsilon^i].$$

The evolution equation (9) lets ε^i evolve towards local minimizers of Φ_N. We are interested in the limit $v\to0$ which amounts to infinitely fast evolution such that $\varepsilon(u_N)$ attains a local minimizer of Φ_N. First we construct the equilibrium points. Inside the i-th spring element, the strain must satisfy the condition $V'(\varepsilon^i)=\sigma$. For given total stress σ, there are at most the three local minimizers

$$\check{\varepsilon}_a=\frac{\sigma}{k_0+\sigma},\quad \check{\varepsilon}_b=\frac{\sigma-\sigma_a}{k_b}+\varepsilon_a,\quad \check{\varepsilon}_c=\frac{\sigma(1+\varepsilon_*)+k_0\varepsilon_*}{k_0+\sigma}=\check{\varepsilon}_a+\varepsilon_*.$$

Let p, q, $1-p-q$ denote the phase fractions of the minimizers a, b, and c, which corresponds to having Np, Nq, $N(1-p-q)$ springs in phase a, b, and c, respectively.

As $\varepsilon\mapsto V(\varepsilon)$ is concave in Regime b, if the elongation of a spring in the local minimum $\check{\varepsilon}_b$ is altered by an arbitrarily small perturbation, it will move (according to the sign of the perturbation) to either $\check{\varepsilon}_a$ or $\check{\varepsilon}_c$. In consequence, any system of N springs with $q\neq0$ is unstable and we may in the following restrict to the case $q=0$.

From $\varepsilon=p\check{\varepsilon}_a+(1-p)\check{\varepsilon}_c$ we compute the equilibrium stress–strain relation to be

$$\sigma(\varepsilon)=\frac{k_0(\varepsilon-\varepsilon_p)}{1-(\varepsilon-\varepsilon_p)}, \tag{10}$$

with

$$\varepsilon_p:=(1-p)\varepsilon_*,$$

that can in a natural way be identified with the plastic strain. From (10) we see that σ only depends on the elastic strain $\varepsilon_{\mathrm{el}}:=\varepsilon-\varepsilon_p$.

For the energy of the equilibrium configuration with Np springs in phase a we find

$$\hat{E}_p(\varepsilon)=-k_0\left[\frac{\sigma(\varepsilon)}{k_0+\sigma(\varepsilon)}+\ln\left(\frac{k_0}{k_0+\sigma(\varepsilon)}\right)\right]+(1-p)c_2=-k_0[(\varepsilon-\varepsilon_p)+\ln(1-(\varepsilon-\varepsilon_p))]+(1-p)c_2.$$

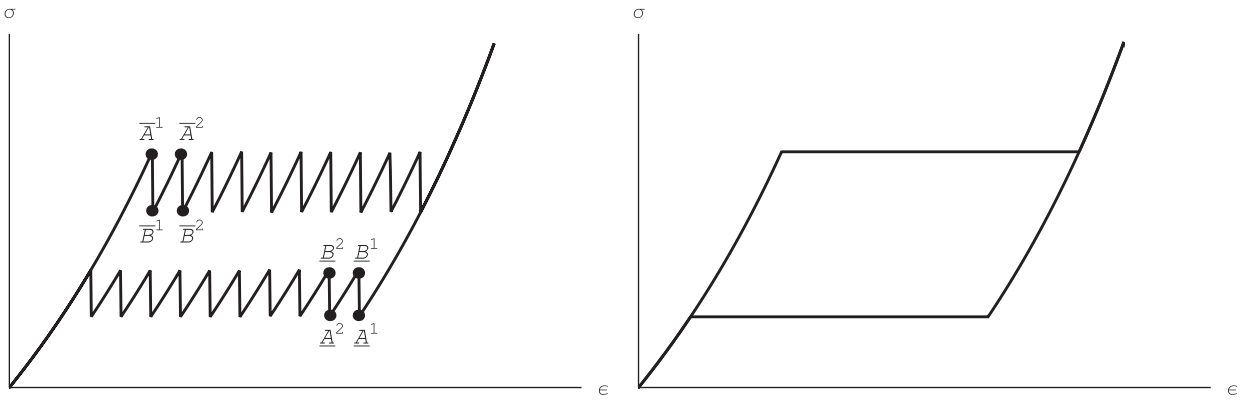

Fig. 4. Overall stress–strain pattern for a chain with $N=10$ microscopic springs (left), and limit response for $N\to\infty$ (right).

Note that $\hat{E}_p$ has a finite number of local minimizers (depending on the remaining parameter p). As explained in Puglisi and Truskinovsky (2005), the switching takes place between branches that differ in exactly one element in the phase state and the succession of N such steps describes the transition from one homogeneous state to the next. Each of these steps can be thought of as the combination of an elastic part and a plastic part.

The stress–strain curve of the foam follows a sawtooth pattern as illustrated in Fig. 4 (left). We denote by $\overline{A}^i$ the end point of the i-th branch. The $\overline{A}^i$ are the final states of the *elastic steps* ($\overline{B}^i\to\overline{A}^{i+1}$) where the system remains on the same metastable branch as long as possible. The *plastic steps* ($\overline{A}^i\to\overline{B}^i$) are characterized by that the total strain is fixed and the system switches between metastable branches that are neighbors ($[Np]=1$, and $[Q]$ generically denotes the jump of a quantity Q). These considerations lead to the representation

$$\overline{A}^i=\left(\varepsilon_{\overline{A}_i},\frac{k_0\varepsilon_a}{1-\varepsilon_a}\right),\quad \overline{B}^i=\left(\varepsilon_{\overline{A}_i},\frac{k_0(\varepsilon_a-\varepsilon_*/N)}{1+\varepsilon_*/N-\varepsilon_a}\right),\quad 1\le i\le N$$

in the $(\varepsilon,\sigma)-$diagram, where

$$\varepsilon_{\overline{A}_i}:=\varepsilon_a+\frac{i-1}{N}\varepsilon_*. \tag{11}$$

So we can compute that a plastic step is characterized by

$$[\varepsilon]=0,\quad [Np]=1,\quad [\sigma]=-\frac{k_0\varepsilon_*}{N(1-\varepsilon_a)(1+\varepsilon_*/N-\varepsilon_a)},$$

whereas an elastic step fulfills

$$[\varepsilon]=\frac{\varepsilon_*}{N},\quad [Np]=0,\quad [\sigma]=+\frac{k_0\varepsilon_*}{N(1-\varepsilon_a)(1+\varepsilon_*/N-\varepsilon_a)}.$$

The evolution equation (9) lets ε^i evolve towards local minimizers of Φ_N. Now we want to look at the energetics of the plastic and the elastic regime. For an elastic step we have the energy difference

$$\Delta\hat{E}_N=k_0[\ln(1-\varepsilon_a)-\ln(1-\varepsilon_a+\varepsilon_*/N)]+\frac{k_0\varepsilon_*+c_2}{N}.$$

In the same spirit, we calculate that for a system with $N\ge 1$ springs, the plastic dissipation is

$$D_N:=k_0[\ln(1-\varepsilon_a+\varepsilon_*/N)-\ln(1-\varepsilon_a)]-\frac{c_2+k_0\varepsilon_*}{N}=k_0\frac{1}{\xi_N}\frac{\varepsilon_*}{N}-\frac{c_2+k_0\varepsilon_*}{N}\quad\text{for a }\xi_N\in(1-\varepsilon_a,1-\varepsilon_a+\varepsilon_*/N). \tag{12}$$

Clearly, $\xi_N\to 1-\varepsilon_a$ for $N\to\infty$.

In one hysteresis cycle, there are N loading steps and N steps when the system is unloaded, so we have totally $2N$ steps that dissipate energy. The total dissipated energy D in a cycle becomes in the limit $N\to\infty$

$$D=\lim_{N\to\infty}2ND_N=\left|\frac{2k_0\varepsilon_*\varepsilon_a}{1-\varepsilon_a}-2c_2\right|. \tag{13}$$

We put the modulus here to ensure that the dissipation is positive.

The limit stress–strain pattern for $N\to\infty$ is shown in Fig. 4. It corresponds to a "perfectly plastic" behavior with stress plateaux at $\sigma=\sigma_a=k_0\varepsilon_a/(1-\varepsilon_a)$ (loading plateau) and $\sigma=\sigma_c=\sigma_a+\Delta\sigma$ (unloading plateau). We emphasize again that this ansatz only works for rate-independent plasticity where the energy only depends on start point and end point of the evolution, but not on the evolution path itself. The limit dissipation (13) equals the area enclosed by the limit stress–strain response. As already observed, we confer the behavior shown in Fig. 4 (right) to a mesoscopic spring element, which represents a finite portion of the CNT foam thickness.

4. Multiscale numerical modeling

We formulate in the present section a multiscale numerical model of a nonlinear mass-spring chain, where each spring represents either a microscopic bi-stable element (cf. Section 2), or a mesoscopic dissipative element of the kind introduced in the previous section. We introduce two different time scales: an external (slow) time $\tau \in [\tau_0,\tau_1]$ ruling an evolution law of the applied boundary conditions, and an internal (fast) time $t \in [t_0,t_1]$ governing the dynamic relaxation of the system for fixed τ. Depending on the adopted model for the individual springs, we may have that the t corresponds to the microscopic time scale (i.e. to the time ruling the microscopic behavior) and τ to the mesoscopic time (micro–meso transition), or, alternatively, that t corresponds to the mesocopic time and τ to the macroscopic time (meso–macro transition).

Let us denote a prescribed displacement time-history of the topmost mass m^N by $\delta(\tau)$. We introduce a discretization $\{\tau_1,\ldots,\tau_M\}$ of the loading interval $[\tau_0,\tau_1]$ and compute the system response for fixed $\tau=\tau_k$ and $\overline{\delta}=\delta(\tau_k)$, through integration with respect to t of the evolution equations

$$m^i \ddot{\hat{u}}^i_N + \gamma^i \dot{\hat{u}}^i_N = \sigma^{i+1} - \sigma^i, \quad i=1,\ldots,N, \tag{14}$$

which generalize the gradient flow equations (9). In (14), $\hat{u}^i_N = \hat{u}^i_N(t)$ denote transient displacement histories of the masses $m^0,\ldots,m^N$ at fixed τ; σ^i indicates the current stress in the ith spring (it is understood that it results $\sigma^i=0$ for $i>N$); and $\gamma^1,\ldots,\gamma^N$ denote damping coefficients.

Since we are only interested in the final equilibrium configuration of the transient internal motion, we 'overdamp' such a motion by introducing fictitious masses and damping factors in (14). In detail, we set the integration time step Δt to unity and introduce fictitious masses $m^i=\alpha k^i \Delta t^2$, with $k_i = h_N(V^i+V^{i+1})''$ and $\alpha \geq 100$. This ensures $\Delta t \leq 0.1\sqrt{m^i/k^i}$ ($i=1,\ldots,N$) (Fraternali et al., 2010). Moreover, we let the generic γ^i be equal to the 'critical' damping defined by

$$\gamma^i = 2\sqrt{m^i k^i}. \tag{15}$$

The equations of motion (14) are associated with the initial conditions

$$\hat{u}^i_N(t=t_0) = (u^i_N)^{(k-1)}, \quad i=0,\ldots,N-1, \quad \hat{u}^N_N(t=t_0)=\overline{\delta}$$
$$\dot{\hat{u}}^i_N(t=t_0)=0, \quad i=0,\ldots,N, \tag{16}$$

where $(u^i_N)^{(k-1)}$ ($i=1,\ldots,N$) are the displacements of the masses at the external time $\tau=\tau_{k-1}$. Eqs. (14), (16) are numerically integrated through a fourth-order Runge–Kutta integration scheme, up to an internal time t_1 such that it results $|\sigma^{i+1}-\sigma^i| \leq 10^{-6}|\sigma^N|$ for all $i \in \{1,\ldots,N-1\}$. When the internal equilibrium is reached, we set $k \leftarrow k+1$ and re-iterate problem (14).

For the micro–meso convergence study of Section 5.1, we consider the stress–strain law described by Eq. (6) and illustrated in Fig. 3 for each microscopic spring. For the simulation of compression tests on real CNT foams, we instead adopt non-uniform chains of mesoscopic springs characterized by a suitable numerical regularization of the stress–strain

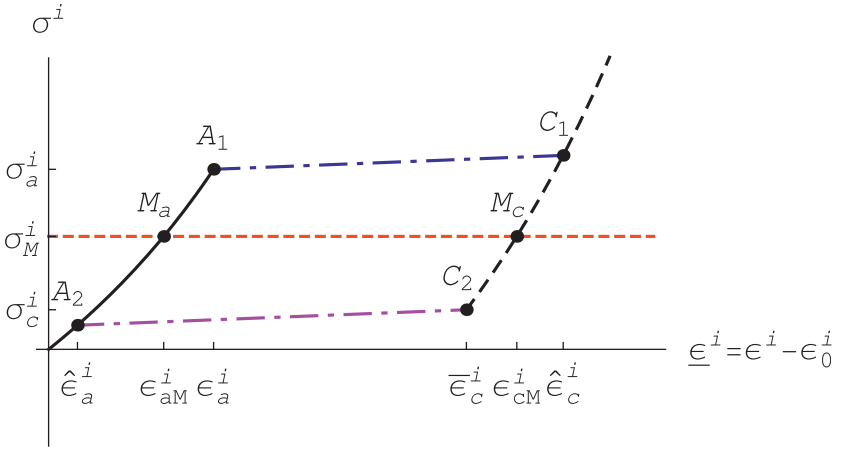

Fig. 5. Hardening-type regularization of the mesoscopic response.

pattern shown in Fig. 4. In detail, we introduce a 'hardening' type regularization consisting of the following stress–strain law (Fig. 5)

$$\sigma^i=\begin{cases}\sigma^{(a,i)}=k_0^i\underline{\varepsilon}_i/(1-\underline{\varepsilon}^i), & (\underline{\varepsilon}^i<\hat{\varepsilon_a}^i)\quad\text{or}\quad((\hat{\varepsilon_a}^i<\underline{\varepsilon}^i<\varepsilon_a^i)\quad\text{and}\quad(\text{flag}^{(k-1)}\neq c)),\\ \sigma^{(d,i)}=\sigma_a^i+k_{h+}^i(\underline{\varepsilon}^i-\varepsilon_a^i), & (\varepsilon_a^i\le\underline{\varepsilon}^i\le\hat{\varepsilon}_c^i)\quad\text{and}\quad(\text{flag}^{(k-1)}=a),\\ \sigma^{(e,i)}=\sigma_a^i+\Delta\sigma^i+k_{h-}^i(\underline{\varepsilon}^i-\overline{\varepsilon}_c^i), & (\hat{\varepsilon}_a^i\le\underline{\varepsilon}^i\le\overline{\varepsilon}_c^i)\quad\text{and}\quad(\text{flag}^{(k-1)}=c),\\ \sigma^{(c,i)}=k_c^i(\underline{\varepsilon}^i-\varepsilon_*^i)/(1-(\underline{\varepsilon}^i-\varepsilon_*^i)), & (\underline{\varepsilon}^i>\hat{\varepsilon_c}^i)\quad\text{or}\quad((\overline{\varepsilon}_c^i<\underline{\varepsilon}^i<\hat{\varepsilon}_c^i)\quad\text{and}\quad(\text{flag}^{(k-1)}\neq a)),\end{cases}\tag{17}$$

where for each $\tau=\tau_k$ (k=1, …, M), we set

$$\text{flag}^{(k)}=\begin{cases}a, & (\underline{\varepsilon}^i<\hat{\varepsilon_a}^i)\quad\text{or}\quad((\hat{\varepsilon_a}^i<\underline{\varepsilon}^i<\varepsilon_a^i)\quad\text{and}\quad(\text{flag}^{(k-1)}\neq c)),\\ c, & (\underline{\varepsilon}^i>\hat{\varepsilon_c}^i)\quad\text{or}\quad((\overline{\varepsilon}_c^i<\underline{\varepsilon}^i<\hat{\varepsilon}_c^i)\quad\text{and}\quad(\text{flag}^{(k-1)}\neq a)),\\ \text{flag}^{(k-1)}, & \text{otherwise.}\end{cases}\tag{18}$$

The quantities $k_0^i,\Delta\sigma^i,k_c^i,\varepsilon_i^a,\varepsilon_c^i,k_{h+}^i$ and k_{h-}^i in (17) are constitutive parameters (seven independent parameters), while $\hat{\varepsilon}_a^i$ and $\hat{\varepsilon}_c^i$ are computed by solving for ε^i the equations

$$\sigma^{(a,i)}=\sigma^{(e,i)},\quad \sigma^{(c,i)}=\sigma^{(d,i)},\tag{19}$$

respectively. One gets back to a perfectly plastic mesoscopic response by setting the regularization ('hardening') parameters k_{h+}^i and k_{h-}^i equal to zero. The quantities ε^i are given by (2) under the replacement of u_N^i with $\hat{u}_N^i$.

5. Applications

The present section deals with applications of the above numerical model to a convergence study and the fitting of laboratory tests on the cyclic compression of CNT foams. In the first case, series of springs with constitutive Eq. (6) were considered (model # 1: micro–meso transition), letting the total number of springs of the system increase progressively (micro–meso transition). In the second case, springs corresponding to Eq. (17) were examined instead (model # 2: meso–macro transition). The optimal fit of available experimental stress–strain curves was performed by varying the constitutive parameters of Eq. (17) and the number of mesoscopic springs N. Depending on the value of N, a significant number of parameters may need to be identified. This lead us to employ a fitting procedure based on genetic algorithms, which have been proved to be well-suited for multi-modal non-convex optimization (cf. e.g. El Sayed et al., 2008; Fraternali et al., 2010). In all the examined examples, we name *global strain* the quantity $\varepsilon=(L-\ell)/L$, ℓ denoting the total deformed length of the chain.

5.1. Convergence study and micromechanics of 'plastic' steps

We examined uniform chains with fixed length $L=860\,\mu$m and increasing number of microscopic springs N, subject to a complete loading–unloading compression cycle up to a global strain $\varepsilon=0.85$ (as in the experiments examined in Section 5.2.2). We employed model #1 with k_c=k_0 ('symmetric' case); $\varepsilon_0=0$; and the material properties listed in Table 1 of the Appendix for all the springs. Fig. 6 shows the numerically computed dissipation D_N versus strain ε and stress σ versus ε responses of such a model for different numbers of springs (N=5, 10, 15 and 50). The $\sigma-\varepsilon$ plot in Fig. 6 highlights that the global stress–strain response alternates elastic steps and 'plastic' jumps of σ at constant ε, oscillating converging to the 'perfectly plastic' mesoscopic behavior shown in Fig. 4. The $D_N-\varepsilon$ plot in Fig. 6 instead shows that D_N converges to the limit dissipation defined in Eq. (13). The above results therefore confirm the theoretical predictions of Section 3. Selected equilibrium configurations and a deformation animation (online version only) of the model with N=5 springs are given in Fig. 7. One can easily recognize the configurations corresponding to the plastic steps of the microscopic chain, displaying the snap of a single spring and the simultaneous elastic rearrangement of the remaining springs (cf., e.g., configurations 3 and 5 from the left). It is worth noting that the ordering of the springs is of no relevance in the present case. Therefore, the succession of the spring snaps can indifferently proceed from the bottom to the top of the chain, as shown in Fig. 7, from top to bottom, or in random sequence. In a real-world chain of springs, the parameters as k_0 or ε_a would never be perfectly identical and the small deviations of the different springs would break the symmetry and determine the ordering when the springs snap.

5.2. Fitting of experimental results on compressed CNT foams

We examined the experimental results of a cyclic compression test on a doubly-anchored CNT foam run at the Graduate Aerospace Laboratories of the California Institute of Technology, and the results given in Cao et al. (2005) on the cyclic compression of a foam-like CNT film. We fit model # 2 both to the first loading/unloading cycle of the examined foams, and to selected cycles following an initial mechanical preconditioning, employing the Breeder Genetic Algorithm (BGA) presented in the Appendix. For the fit of the first cycles we assumed $\varepsilon_0^i=0$ in each spring, while for the cycles following the

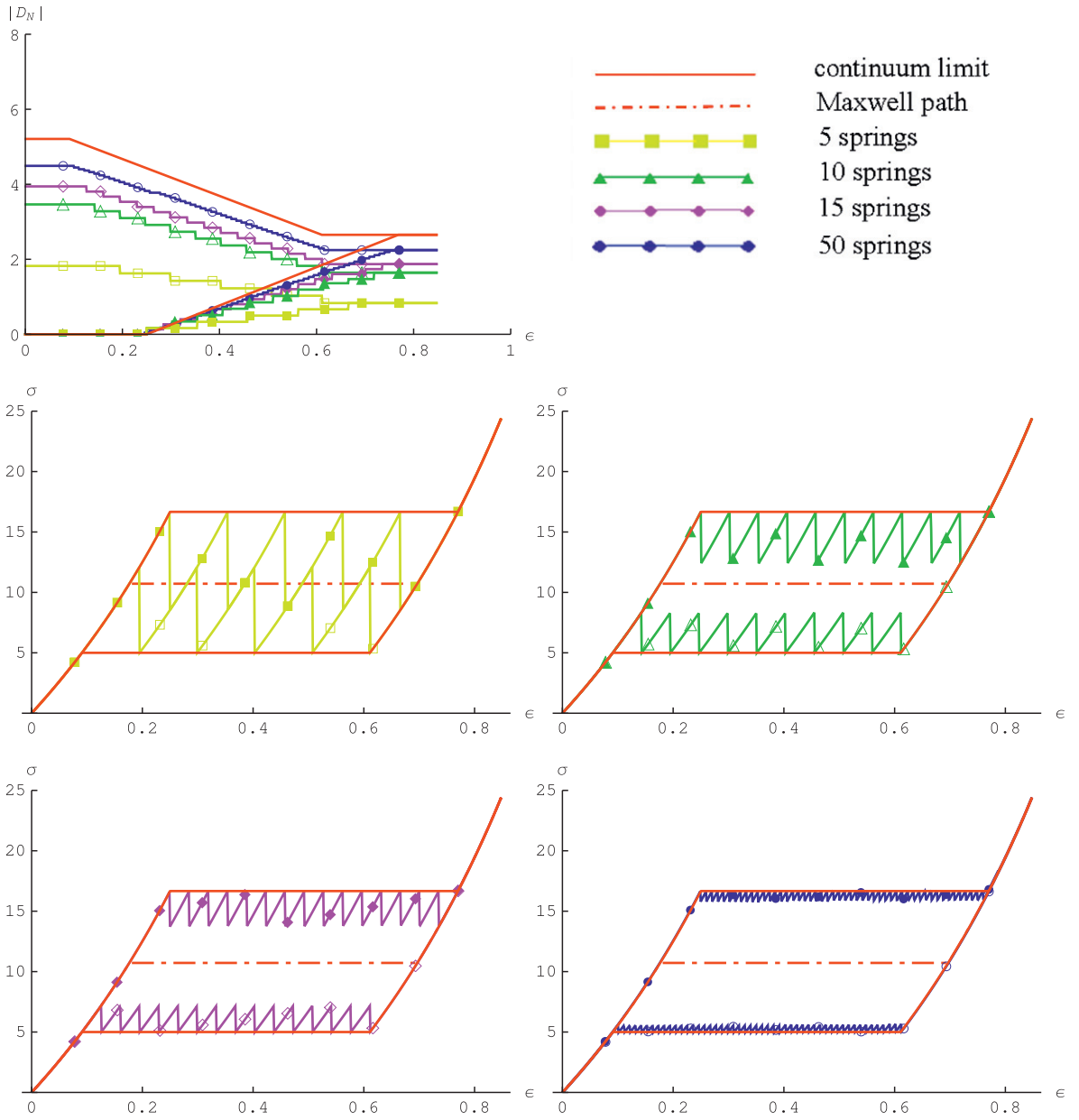

Fig. 6. Response of uniform chains of microscopic bi-stable springs with properties shown in Table 1 of the Appendix: D_N dissipation (kJ/m^2); σ global stress (MPa); ε global strain (filled marks: loading; unfilled marks: unloading).

foam preconditioning we set $\varepsilon_0^i = \varepsilon_0$ in each spring, ε_0 being the macroscopic (permanent or transient) strain observed at zero stress at the end of the previous loading cycle. For the cycles following the preconditioning, we considered two different fitting models: one accounting for hysteresis (numerical (1): $\Delta\sigma^i < 0$ in each mesoscopic spring), and the other one without hysteresis (numerical (2): $\Delta\sigma^i = 0$ in each mesoscopic spring). Since all the adopted fitting models account for macroscopic time-independent behavior (cf. Section 3), our fitting results are independent of the strain rate actually applied in the experiments.

5.2.1. Compression tests on a doubly-anchored CNT foam

We performed cyclic compression tests on vertically aligned multi-walled carbon nanotube forests (800 μm in length with sample area $\sim 14\,\text{mm}^2$) grown by chemical vapor deposition (CVD) using ferrocene and toluene as precursors. The average diameter of the as-grown CNTs was $\sim 50\,\text{nm}$. The as-grown CNT foams were partially anchored between two polymer layers to provide structural support and sample transportability.

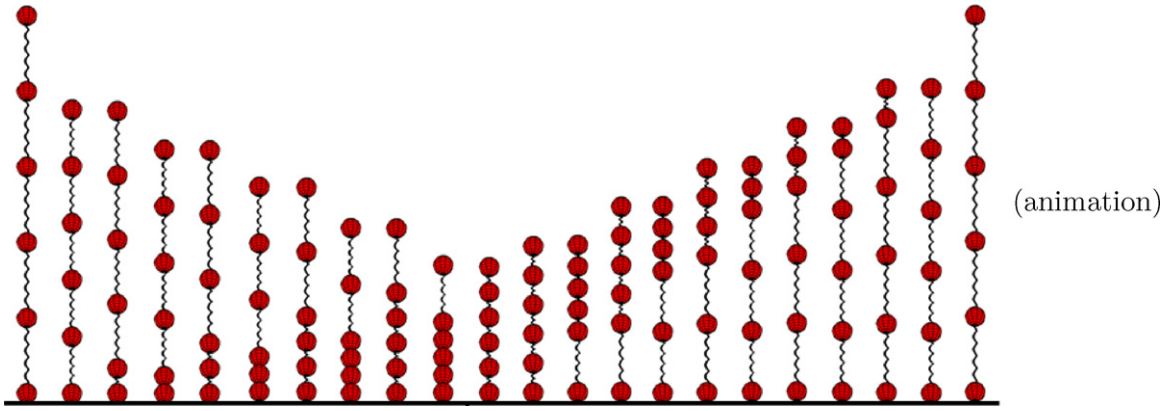

Fig. 7. Selected equilibrium configurations (left) and deformation animation (right-online version only) of the model described in Table 1 of the Appendix, for $N=5$.

For anchoring the CNT foams on a substrate we spin-coated polydimethylsiloxane (PDMS) on top of a glass slide at 800 RPM to get $50-100\,\mu m$ thick films. Before curing the polymer we partially embedded the CNT-foams at 80 °C for 1 h. After curing, the carbon nanotubes protruding from the substrate showed excellent vertical alignment with an average height of $\sim 750\,\mu m$. The process was repeated turning the sample upside down to obtain a 'doubly anchored' system (i.e. sandwich structure with polymer on both sides and the CNT foam in the middle). Typical experimental results obtained from cyclic compression tests are shown in Fig. 8 (top).

We separately fit the first and the fourth stress–strain cycles shown in Fig. 8 to model # 2, considering the general 'asymmetric' case with $k_c^i \neq k_0^i$ ($i=0,\ldots,N-1$) and a chain with $N=4$ springs. For the fourth cycle we accounted for an initial strain $\varepsilon_0 = 0.20$, which approximatively corresponds to the strain measured at zero stress at the end of the third loading cycle (Fig. 8, top). The best fit parameters obtained through BGA optimization are given in Table 2 of the Appendix. A comparison between best-fit and experimental overall stress–strain curves is shown in Fig. 8 (center and bottom). One observes that the non-uniform dissipative mass-spring model is able to capture the real hysteretical behavior of the examined CNT foam, both at their pristine state (first cycle) and after mechanical preconditioning (fourth cycle), through a multi-plateaux overall stress–strain profile. In particular, Fig. 8-bottom and Table 2 of the Appendix show that the response after preconditioning can be roughly described through a suitable non-dissipative model.

5.2.2. Compression tests on a foamlike CNT film

We fit a cyclic compression test given in Cao et al. (2005) for a CNT foam-like film with thickness $L = 860\,\mu m$. The analyzed experiment performed 1000 loading/unloading cycles up to a global strain $\varepsilon = 0.85$ (cf. Fig. 3B of Cao et al., 2005 and Fig. 3 of the Appendix). The fitting of the 'symmetric' formulation of model # 2 ($k_c^i = k_0^i$ in each spring) to the first cycle is presented in the Appendix. A dramatic improvement of the fitting ability of model # 2 was obtained by considering the 'asymmetric' case ($k_c^i \neq k_0^i$). As shown in Table 4 of the Appendix, we were indeed able to reduce the fitting fitness to 0.808 MPa by using a BGA-optimized "asymmetric" multiscale model with 10 springs. Such a fitness value is markedly lower than that obtained for the corresponding "symmetric" case (1.462 MPa, cf. Table 3 of the Appendix). We were also able to optimally fit the 1000th cycle of the examined experiment to the 'asymmetric' model, obtaining a fitting fitness of 0.444 MPa through the BGA-optimized 5 spring model described in Table 4 of the Appendix. The excellent match between numerical and experimental results for the present case is illustrated by Fig. 9, which compares predicted and measured overall stress–strain responses. For the first cycle we observe that the numerical multi-plateaux response closely approaches the continuous experimental recording as the number of mesoscopic springs increases from 5 to 10 (Fig. 9, top and center). Regarding the 1000th cycle, we assumed $\varepsilon_0 = 0.14$ (cf. Cao et al., 2005). Fig. 9, bottom shows that the experimental stress–strain profile corresponding to the 1000th cycle is already excellently approximated by a 5 spring model with dissipation (numerical (1)), and roughly described by an analogous model without dissipation (numerical (2)). One observes from Tables 3 and 4 of the Appendix that the average value of the stiffness k_0^i among all springs is approximatively equal to the elastic modulus estimated by Cao et al. (2005) for the present CNT foam (≈ 50 MPa).

6. Discussion and outlook

In this article we derived a mechanical model describing the behavior of CNT foams under uniform compression, through the concept of bi-stable springs presented in Puglisi and Truskinovsky (2000, 2002, 2005), which has been recently applied to open-cell polyurethane foams (Pampolini and Del Piero, 2008).

The proposed model differs from other bi-stable mass-spring models available in the literature (refer e.g. to Blesgen, 2007; Braides and Cicalese, 2007; Charlotte and Truskinovsky, 2002, 2008; Ortiz, 1999; Puglisi and Truskinovsky, 2000,

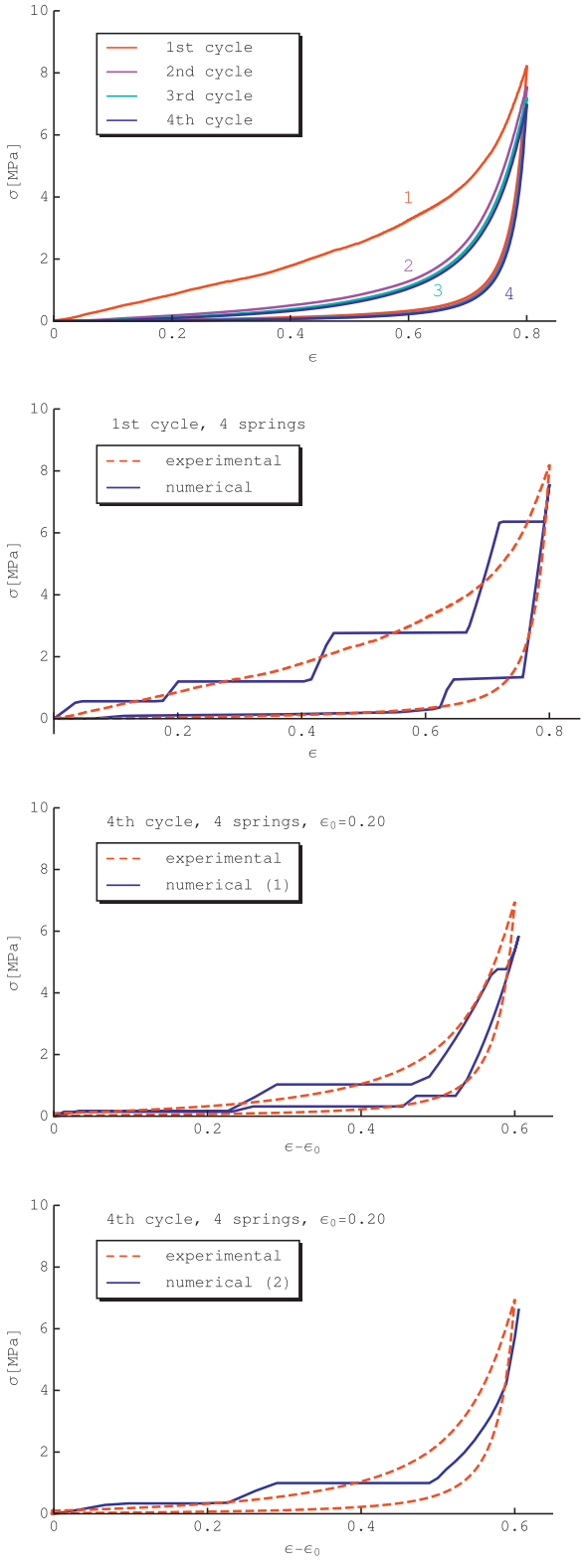

Fig. 8. Fitting of compression tests on a doubly-anchored CNT foam (top) to non-uniform 'asymmetric' spring models (properties in Table 2 of the Appendix).

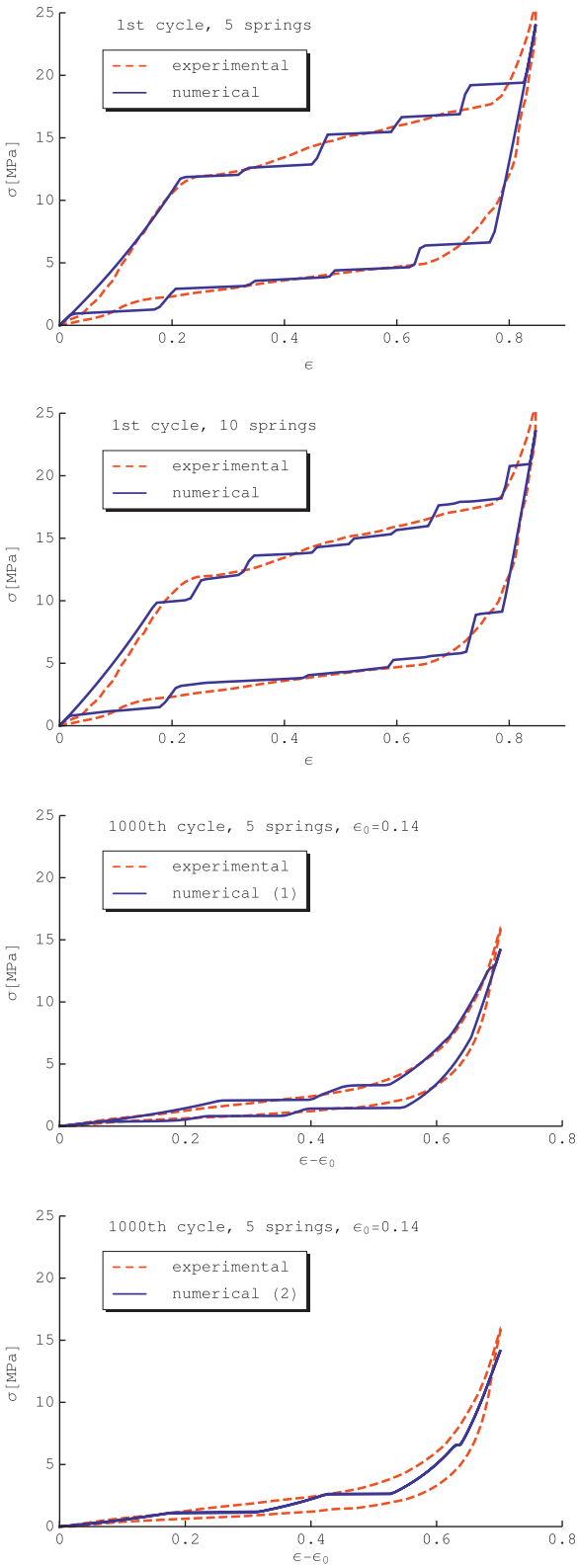

Fig. 9. Fitting of experimental compressive stress–strain curves of CNT foams (Cao et al., 2005) to non-uniform 'asymmetric' spring models (properties in Table 4 of the Appendix).

2002, 2005, and references therein), due to the presence of an intermediate, mesoscopic scale, placed in between the microscopic scale of the bi-stable springs, and the macroscopic scale of the entire structure. The microscopic scale aims to describing the dynamic snapping of the carbon nanotubes due to local buckling (Cao et al., 2005; Zbib et al., 2008; Misra et al., 2009; Hutchens et al., 2010), while the mesoscopic scale is intended to describe the time-independent hysteretic behavior of finite portions of the CNT foam. The latter typically follows from kinking, sticking and entanglement of the tubes, friction and other microscopic dissipative effects (Suhr et al., 2007; Teo et al., 2007; Tong et al., 2008; Deck et al., 2007; Misra et al., 2009).

Another relevant difference between the present model and most of the available bi-stable mass-spring models consists of the fact that the current model accounts for non-uniform mesoscopic spring properties, while other models usually consider uniform chains of bi-stable springs (see e.g. Puglisi and Truskinovsky, 2000, 2002; Pampolini and Del Piero, 2008). Such a mechanical inhomogeneity allows us to account for hardening of the macroscopic response in the post-buckling range (Cao et al., 2005; Misra et al., 2009).

The numerical results given in Section 5 demonstrated that our methods are capable of recovering available experimental results on the compression of CNT foams with excellent agreement. We fitted the parameters of the mesoscopic springs through a Breeder Genetic Algorithm, which is well-suited for global non-convex optimization. The fitting of experimental stress–strain curves allowed us to recognize that non-uniform dissipative mass-spring models are well-suited to capture the main features of the real compressive response of CNT foams, and specifically strain localization due to CNT kinking and time-independent hysteresis. The latter was found to be relevant during loading/unloading from the pristine state, and progressively decaying after mechanical preconditioning. By setting to zero the dissipation of the model, we were led to obtain a rough, non-linearly elastic approximation of the examined experimental behaviors after preconditioning.

The distinctive features of the multiscale model presented in this work highlight its potential use to describing the mechanical behavior of multilayered systems composed of alternating CNT foams and anchoring polymeric films (Misra et al., 2009). We will address such an extension of the current model in future work. Other future directions of the present research might regard the description of permanent deformation through fatigue or damage mechanisms; the inclusion of rate-dependent dissipative effects at the macroscopic scale; and the modeling of long-range interactions mimicking van der Waals forces.

Acknowledgements

The authors would like to thank Dr. Abha Misra and Dr. Luigi de Nardo for performing the experiments presented in Section 5.2.1. CD acknowledges support from the Institute for Collaborative Biotechnologies under contract W911NF-09-D-0001 with the Army Research Office. FF greatly acknowledges the support of the University Centre for Risk Prediction and Prevention (CUGRI) in association between the Universities of Salerno and Napoli "Federico II", Italy. FF also thanks the Graduate Aerospace Laboratory at the California Institute of Technology (GALCIT) for the hospitality during his visit.

Appendix A. Supplementary data

Supplementary data associated with this article can be found in the online version at doi:10.1016/j.jmps.2010.09.004.

References

Arroyo, M., Belytschko, T., 2003. A finite deformation membrane based on inter-atomic potentials for the transverse mechanics of nanotubes. Mech. Mater. 35 (23), 193–215.
Belytschko, T., Xiao, S.P., Schatz, G.C., Ruoff, R.S., 2002. Atomistic simulations of nanotube fracture. Phys. Rev. B 65, 235430.
Blesgen, T., 2007. On the competition of elastic energy and surface energy in discrete numerical schemes. Adv. Comput. Math. 27 (2), 179–194.
Braides, A., Cicalese, M., 2007. Surface energies in nonconvex discrete systems. Math. Mod. Mrth. Appl. Sci. 17 (7), 985–1037.
Cao, A., Dickrell, P.L., Sawyer, W.G., Ghasemi-Nejhad, M.N., Ajayan, P.M., 2005. Super-compressible foamlike carbon nanotube films. Science 310, 1307–1310.
Cao, G., Chen, X., 2006. Buckling of single-walled carbon nanotubes upon bending: molecular dynamics simulations and finite element method. Phys. Rev. B 73, 155435.
Chan, S.-P., Yim, W.-L., Gong, X.G., Liu, Z.F., 2003. Carbon nanotube bundles under high pressure: transformation to low-symmetry structures. Phys. Rev. B 68, 075404.
Charlotte, M., Truskinovsky, L., 2002. Linear elastic chain with a hyper-pre-stress. J. Mech. Phys. Solids 50 (2), 217–251.
Charlotte, M., Truskinovsky, L., 2008. Towards multi-scale continuum elasticity theory. Cont. Mech. Therm. 20 (3), 133–161.
Chesnokov, S.A., Nalimova, V.A., Rinzler, A.G., Smalley, R.E., Fisher, J.E., 1999. Mechanical energy storage in carbon nanotube springs. Phys. Rev. Lett. 82 (2), 343–346.
Daraio, C., Nesterenko, V.F., Aubuchon, J.F., Jin, S., 2004a. Dynamic nano-fragmentation of carbon nanotubes. Nano Lett. 4 (10), 1915–1918.
Daraio, C., Nesterenko, V.F., Jin, S., 2004b. Highly nonlinear contact interaction and dynamic energy dissipation by forest of carbon nanotubes. Appl. Phys. Lett. 85 (23), 5724–5727.

Daraio, C., Nesterenko, V.F., Jin, S., Wang, W., Rao, A.M., 2006. Impact response by a foamlike forest of coiled carbon nanotubes. J. Appl. Phys. 100 (6), 064309–064309-4.
Deck, C.P., Flowers, J., McKee, G.S.B., Vecchio, K., 2007. Mechanical behavior of ultralong multiwalled carbon nanotube mats. J. Appl. Phys. 101 (2), 023512–023512-9.
Deck, C.P., Vecchio, K.S., 2005. Growth of well-aligned carbon nanotube structures in successive layers. J. Phys. Chem. B 109 (25), 12353–12357.
El Sayed, T., Mota, A., Fraternali, F., Ortiz, M., 2008. A variational constitutive model for soft biological tissues. J. Biomech. 41 (7), 1458–1466.
Falvo, M.R., Clary, G.J., Taylor, R.M., Chi, V., Brooks Jr., F.P., Washburn, S., Superfine, R., 1997. Bending and buckling of carbon nanotubes under large strain. Nature 389, 582–584.
Fraternali, F., Porter, M.A., Daraio, C., 2010. Optimal design of composite granular protectors. Mech. Adv. Mater. Struct. 17 (1), 1–19.
Gibson, L.J., Ashby, M.F., 1998. Cellular Solids: Structure and Properties. Pergamon Press, Oxford.
Hutchens, S.B., Hall, L.J., Greer, J.R., 2010. In situ mechanical testing reveals periodic buckle nucleation and propagation in carbon nanotube bundles. Adv. Funct. Mater. 20 (14), 2338–2346.
Iijima, S., 1991. Helical microtubules of graphitic carbon. Nature 354, 56–58.
Iijima, S., Brabec, C., Maiti, A., Bernholc, J., 1995. Structural flexibility of carbon nanotubes. J. Chem. Phys. 104 (5), 2089–2092.
Liu, J.Z., Zheng, Q.-S., Wang, L.-F., Jiang, Q., 2005. Mechanical properties of single-walled carbon nanotube bundles as bulk materials. J. Mech. Phys. Solids 53 (1), 123–142.
Liu, Y., Qian, W., Zhang, Q., Cao, A., Li, Z., Zhou, W., Ma, Y., Wei, F., 2008. Hierarchical agglomerates of carbon nanotubes as high-pressure cushions. Nano Lett. 8 (5), 1323–1327.
Maheshwari, V., Saraf, R., 2008. Tactile devices to sense touch on a par with a human finger. Angew. Chem.-Int. Ed. 47 (41), 7808–7826.
Majumder, M., Chopra, N., Andrews, R., Hinds, B.J., 2005. Enhanced flow in carbon nanotubes. Nature 438 (44) Angewandte Chemie-International Edition 47(41), 7808–7826.
Mesarovic, S.Dj., McCarter, C.M., Bahr, D.F., Radhakrishnan, H., Richards, R.F., Richards, C.D., McClain, D., Jiao, J., 2007. Mechanical behavior of a carbon nanotube turf. Scripta Mater. 56 (2), 157–160.
Misra, A., Greer, J.R., Daraio, C., 2009. Strain rate effects in the mechanical response of polymer-anchored carbon nanotube foams. Adv. Mater. 21 (3), 334–338.
Nesterenko, V.F., 2001. Dynamics of Heterogeneous Materials. Springer-Verlag, NY.
Oberlin, A., Endo, M., Koyama, T., 1976. Filamentous growth of carbon through benzene decomposition. J. Cryst. Grow. 32 (3), 335–349.
Ortiz, M., 1999. Plastic yielding as a phase transition. J. Appl. Mech. 66, 289–298.
Pampolini, G., Del Piero, G., 2008. Strain localization in open-cell polyurethane foams: experiments and theoretical model. J. Mech. Mater. Struct. 3 (5), 969–981.
Pantano, A., Parks, D.M., Boyce, M.C., 2004. Mechanics of deformation of single- and multi-wall carbon nanotubes. J. Mech. Phys. Solids 52 (4), 789–821.
Peters, M.J., McNeil, L.E., Lu, J.P., Kahn, D., 2000. Structural phase transition in carbon nanotubes bundles under pressure. Phys. Rev. B 61 (9), 5939–5944.
Puglisi, G., Truskinovsky, L., 2000. Mechanics of a discrete chain with bi-stable elements. J. Mech. Phys. Solids 48 (1), 1–27.
Puglisi, G., Truskinovsky, L., 2002. Rate independent hysteresis in a bi-stable chain. J. Mech. Phys. Solids 50 (2), 165–187.
Puglisi, G., Truskinovsky, L., 2005. Thermodynamics of rate independent plasticity. J. Mech. Phys. Solids 53 (3), 655–679.
Qi, H.J., Teo, K.B.K., Lau, K.K.S., Boyce, M.C., Milne, W.I., Robertson, J., Gleason, K.K., 2003. Determination of mechanical properties of carbon nanotubes and vertically aligned carbon nanotube forests using nanoindentation. J. Mech. Phys. Solids 51 (11–12), 2213–2237.
Radushkevich, L.V., Lukyanovich, V.M., 1952. O strukture ugleroda, obrazujucegosja pri termiceskom razlozenii okisi ugleroda na zeleznom kontakte (About the structure of carbon formed by thermal decomposition of carbon monoxide on iron substrate). Zurn. Fisic. Chim 26, 88–95.
Suhr, J., Victor, P., Ci, L., Sreekala, S., Zhang, X., Nalamasu, O., Ajayan, P.M., 2007. Fatigue resistance of aligned carbon nanotube arrays under cyclic compression. Nat. Nanotechnol. 2, 417–421.
Teo, E.H.T., Yung, W.K.P., Chua, D.H.C., Tay, B.K., 2007. A carbon nanomattress: a new nanosystem with intrinsic, tunable, damping properties. Adv. Mater. 19 (19), 2941–2945.
Tong, T., Zhao, Y., Delzeit, L., Kashani, A., Meyyappan, M., Majumdar, A., 2008. Height independent compressive modulus of vertically aligned carbon nanotube arrays. Nano Lett. 8 (2), 511–515.
Veedu, V.P., Cao, A., Li, X., Ma, K., Soldano, C., Kar, S., Ajayan, P.M., Ghasemi-Nejhad, M.N., 2006. Multifunctional composites using reinforced laminae with carbon-nanotube forests. Nat. Mater. 5, 457–462.
Yakobson, B.I., Brabec, C.J., Bernholc, J., 1996. Nanomechanics of carbon tubes: Instabilities beyond linear response. Phys. Rev. Lett. 76 (14), 2511–2514.
Zbib, A.A., DjMesarovic, S., Lilleodden, E.T., McClain, D., Jiao, J., Bahr, D.F., 2008. The coordinated buckling of carbon nanotube turfs under uniform compression. Nanotechnology 19 (17), 175704.
Zhang, Q., Zhao, M., Liu, Y., Cao, A., Qian, W., Lu, Y., Wei, F., 2009. Energy-absorbing hybrid composites based on alternate carbon-nanotube and inorganic layers. Adv. Mater. 21 (28), 2876–2880.